Physics of Fluids

RESEARCH ARTICLE | DECEMBER 01 2023

Wings and whiffs: Understanding the role of aerodynamics in odor-guided flapping flight

Menglong Lei (雷梦龙) ; Chengyu Li (李承宇)

Physics of Fluids 35, 121901 (2023)
https://doi.org/10.1063/5.0174377

Physics of Fluids ARTICLE pubs.aip.org/aip/pof

Wings and whiffs: Understanding the role of aerodynamics in odor-guided flapping flight

Cite as: Phys. Fluids **35**, 121901 (2023); doi: 10.1063/5.0174377
Submitted: 30 August 2023 · Accepted: 1 November 2023 ·
Published Online: 1 December 2023

View Online Export Citation CrossMark

Menglong Lei (雷梦龙), and Chengyu Li (李承宇)[a]

AFFILIATIONS

Department of Mechanical Engineering, Villanova University, Villanova, Pennsylvania 19085, USA

[a]Author to whom correspondence should be addressed: chengyu.li@villanova.edu

ABSTRACT

Odor-guided navigation is an indispensable aspect of flying insects' behavior, facilitating crucial activities such as foraging and mating. The interaction between aerodynamics and olfaction plays a pivotal role in the odor-guided flight behaviors of insects, yet the interplay of these two functions remains incompletely understood. In this study, we developed a fully coupled three-way numerical solver, which solves the three-dimensional Navier–Stokes equations coupled with equations of motion for the passive flapping wings, and the odorant advection–diffusion equation. This numerical solver is applied to investigate the unsteady flow field and the odorant transport phenomena of a fruit fly model in odor-guided upwind surge flight over a broad spectrum of reduced frequencies (0.325–1.3) and Reynolds numbers (90–360). Our results uncover a complex dependency between flight velocity and odor plume perception, modulated by the reduced frequency of flapping flight. At low reduced frequencies, the flapping wings disrupt the odor plume, creating a saddle point of air flow near the insect's thorax. Conversely, at high reduced frequencies, the wing-induced flow generates a stagnation point, in addition to the saddle point, that alters the aerodynamic environment around the insect's antennae, thereby reducing odor sensitivity but increasing the sampling range. Moreover, an increase in Reynolds number was found to significantly enhance odor sensitivity due to the synergistic effects of greater odor diffusivity and stronger wing-induced flow. These insights hold considerable implications for the design of bio-inspired, odor-guided micro air vehicles in applications like surveillance and detection.

I. INTRODUCTION

Odor-guided navigation serves as a fundamental behavioral mechanism in flying insects, crucial to a range of activities from foraging to mating.[1–3] Amidst the wide array of environmental cues to which insects must adapt, olfaction holds particular significance for the accurate localization of odor sources.[4] While the study of individual aspects like aerodynamics and olfaction in insects has seen considerable advancement, the complex interplay between these two elements during odor-guided flapping flight has yet to be comprehensively investigated.

Recent advancements in our understanding of insect neuronal mechanisms reveal remarkable capabilities in olfactory dynamics. Olfactory receptor neurons in insects register odorant-evoked spike responses as rapidly as 3 ms following the arrival of an odorant.[5] Notably, the temporal resolution achieved by their antennae can reach frequencies as high as 100 Hz.[6] This exceptional spatiotemporal acuity enables insects to detect dynamic fluctuations in odor plumes. Furthermore, their ability to distinguish differences in odor concentration between their bilateral antennae[7] adds a stereo-olfactory dimension to their navigational toolkit. For instance, hawkmoths adjust their flight paths in accordance with the cross-sectional dimensions of an odor plume,[8] while fruit flies modulate their odor-tracking behavior based on accumulated historical information.[9] In varied environments, mosquitoes[10] and moths[11] have been observed to favor upwind surging flights in intermittently fluctuating plumes over homogeneous, continuous plumes. These findings collectively indicate that insects leverage intricate odor plume information to fine-tune their flight behaviors.

Investigating insect behavior during odor-tracking flight presents significant challenges, one of the foremost being the difficulty in quantitatively visualizing odor plumes at insect-relevant length scales. Existing experimental approaches have largely focused on behavioral observations, which typically reveal that insects zigzag crosswind to engage their olfactory receptors and surge upwind along the odor plume until the source becomes visible.[12] However, the underlying transport mechanisms that explain the purpose of these behaviors remain largely speculative. The previous numerical simulations have also been limited in scope, often failing to provide a comprehensive

view of aerodynamic and olfactory interactions during realistic odor-tracking flight. Most of these simulations have relied on constant boundary conditions,[13,14] which do not account for the dynamic airflow induced by moving wings. To date, it is still unclear how the insects utilize different behaviors to perceive odor plumes perturbed by wing-induced flow.

To understand the behaviors of insects in odor-tracking flight, the most important and complicated yet overlooked organs are the flapping wings which serve two functions, the aerodynamic function and the olfactory function. The aerodynamic function centers on generating the necessary forces and moments to both sustain the insect's body weight and facilitate its spatial locomotion. This aspect has garnered substantial research attention,[15–17] given its relatively straightforward experimental and numerical study procedures. Insect wing kinematics are initially captured using high-speed cameras and subsequently modeled numerically. Solving the Navier–Stokes equations or employing other quasi-steady models then allows researchers to understand the aerodynamics at play. Such aerodynamic functions naturally extend to odor-tracking, as spatial movement allows insects to actively expand their olfactory perception range. However, insect locomotion comes at a significant energetic cost, particularly given the need to maintain constant wing flapping, even during hovering. This implies that insects likely employ more nuanced strategies than merely following a positive odor gradient when navigating odor-guided flight paths. One compelling hypothesis suggests that insects may utilize their wings to fan the air, thereby increasing the flux of odorants reaching their antennae.[18]

Insect wings serve an olfactory function by influencing the odor plume that reaches the antennae through wing-induced airflow. This role was previously identified in silkworms responding to sex pheromones.[19] Odor concentration is spatially heterogeneous. In stagnant or laminar flows, odor plumes disperse, with their concentration diminishing with increasing downwind distance.[20–22] In contrast, turbulent flows fragment the plumes into intermittent filaments, separated by pockets of low or zero concentration. The airflow induced by wing flapping serves to actively draw odor plumes over a broad range toward the antennae, thereby enhancing both air flux and odor perception rates.

Recent advancements in numerical simulations have shed light on the importance of wing-induced airflow in odor perception. Studies by Li and his colleagues[23–26] incorporated the flapping wing kinematics of a fruit fly model into their simulations, allowing for the visualization of odor plume structures during forward flight. These simulations demonstrated that wing flapping disrupts airflow patterns in a manner that elevates the odor flux around the antennae, analogous to the sniffing process in mammals. Importantly, the antennae are strategically positioned to perceive the odor plume while minimizing the influence of wing-induced disturbances. However, it's worth noting that the Lagrangian particle-tracing techniques employed in these studies did not account for the diffusion involved in odorant transport.

Despite the critical role of wing-induced flow in olfaction, the olfactory function of flapping wings has largely been overshadowed by their primary role in aerodynamics to sustain flight. While insects have some capacity to adjust their wing-flapping kinematics,[27,28] any modification aimed at generating specific wing-induced flows could compromise the aerodynamic efficiency, and hence the overall efficacy, of the wings during odor-tracking flight. However, one crucial variable often overlooked in studies of these behaviors is flight velocity. Insects typically zigzag crosswind at lower velocities when searching for an odor plume and transition to higher-velocity, upwind surging once an odor is detected.[12] This nuanced variation in flight velocity has been largely disregarded in previous research, partly because simultaneously measuring odor plumes, controlling flight velocity, and capturing kinematic data presents a considerable experimental challenge due to the insects' small size and the complexity of the flow field.

In this study, we aim to offer a holistic understanding of aerodynamic and olfactory interactions during odor-tracking behavior in insects. To achieve this, we advanced our existing in-house immersed-boundary-method-based computational fluid dynamics (CFD) solver with new computational features. This upgraded three-way coupled solver first resolves the Navier–Stokes equations in conjunction with equations of motion for the passively pitching wings, thereby determining the flow field. Subsequently, the odor advection-diffusion equation is solved at each time step to establish the odor concentration field. We have chosen a fruit fly model for our investigation due to the abundance of experimental data available on its odor-tracking flight and its relatively simplistic wing shape, which minimizes the complications arising from complex wing deformations. To emulate realistic wing kinematics, we prescribed the wing leading-edge motion and stroke-plane angle, while the wing pitch angle was determined using a torsional spring model that incorporates aerodynamic, elastic, inertial, and gravitational forces. Our simulations were conducted in a virtual wind tunnel where the fruit fly model was exposed to a constant air velocity, with an upstream odor source emitting a constant concentration of an odorant. We executed parametric simulations to examine the impact of both reduced frequency and Reynolds number, the results of which are detailed in the ensuing sections.

II. METHODOLOGY

A. Governing equations and numerical method

The three-dimensional viscous incompressible Navier–Stokes equations are solved using an in-house immersed-boundary-method based CFD solver. The equations are written in tensor form,

$$\begin{cases} \dfrac{\partial u_i}{\partial x_i} = 0 \\ \dfrac{\partial u_i}{\partial t} + \dfrac{\partial (u_i u_j)}{\partial x_j} = -\dfrac{1}{\rho}\dfrac{\partial P}{\partial x_i} + \nu \dfrac{\partial}{\partial x_j}\left(\dfrac{\partial u_i}{\partial x_j}\right), \end{cases} \tag{1}$$

where u_i are the velocity component, P is the pressure, ρ is the fluid density, ν is the kinematic viscosity.

The above equations are discretized using a cell-centered, collocated arrangement of the primitive variables, and are solved using a finite difference-based immersed-boundary method[29] in a non-body-conforming Cartesian grid, as shown in Fig. 1. The uppercase letters W, E, N, and S represent cell-centered variables, and the lowercase letters w, e, n, and s represent face-centered variables, which are calculated by interpolating the corresponding cell-centered variables. A second-order central difference scheme is employed in space to discretize the advection and diffusion term. Boundary conditions on the immersed boundaries are imposed through a ghost-cell procedure. The equations are integrated with time using the fractional step method. The immersed-boundary method eliminates the complex remeshing algorithms for moving boundaries on body-conforming

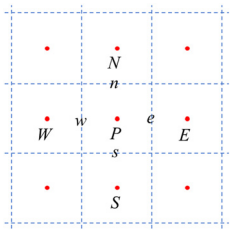

FIG. 1. Schematic of the grid. The uppercase letters denote cell-centered variables, the lowercase letters denote the face-centered variables.

grids at each time step. Our CFD solver has been successfully applied to study canonical revolving wings,[30–33] flapping propulsion problems,[34–38] and insect flight.[24,25,39–42] Details of the CFD solver in solving Navier–Stokes equations were elaborated and validated in our previous studies.[35,39,43–45]

B. Wing model with torsional spring

It has been demonstrated that the insect wing can passively achieve the fundamental kinematic motion due to aerodynamic and wing inertia forces.[46,47] In the current study, the wing pitch angle is calculated using a torsional spring model integrated with the Navier–Stokes CFD solver using a two-way coupling method.[48] As the wing flaps back and forth in the stroke plane with a prescribed stroke angle and the wing root acting like a torsional spring, the wing pitches passively about the wing leading edge. This passive pitching model has been validated with real fruit flies[48] and is used to provide the flapping wing kinematics under varies simulation setups.

The fruit fly model adopted here has been used in our previous studies.[25,26,49] The aspect ratio of the wing is 3.2, defined as $(\text{span})^2/(\text{area})$. As shown in Fig. 2(a), the kinematics of the wing is defined by three Euler angles, stroke (ϕ), and pitch (θ) angle. In Fig. 2(b), the stroke plane angle β is 10°, and the incline angle χ is 45°. This stroke plane angle is specifically chosen by performing a series testing cases so that the drag generated during downstroke approximately balances with the thrust generated during upstroke for the baseline case.

The wing stroke angle is prescribed using Eq. (2), while the wing deviation angle is fixed as zero during the entire flapping motion. The

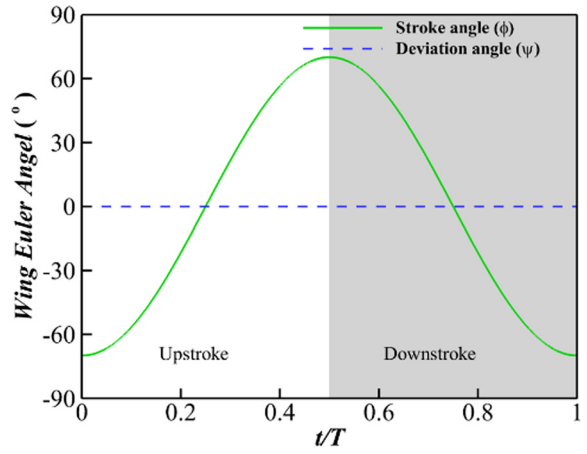

FIG. 3. The time history of prescribed stroke angle and deviation angle. In current study, the stroke amplitude $A_\phi = 140°$, and the deviation amplitude $A_\psi = 0°$. The gray shaded region denotes downstroke.

time history of the prescribed stroke and deviation angle of the wing is shown in Fig. 3,

$$\phi(t) = -A_\phi \cos(2\pi f t), \tag{2}$$

where $\phi(t)$ is the instantaneous wing stroke angle at time t, $A_\phi = 140°$ is the stroke amplitude, and f is the flapping frequency.

At each time step, the instantaneous inertia, aerodynamic, elastic, and gravity momentum are calculated, and the passive pitch angular acceleration of the wings about the wing leading edge is then obtained using the equation of motion, which is written as

$$\begin{aligned} &I_{xx}\dot{\omega}_x + (I_{zz} - I_{yy})\omega_y\omega_z + I_{xy}(\omega_x\omega_z - \dot{\omega}_y) \\ &\quad + I_{yz}(\omega_z^2 - \omega_y^2) - I_{xz}(\dot{\omega}_z + \omega_x\omega_y) \\ &\quad = M_{aero} + M_{elastic} + M_{gravity}, \end{aligned} \tag{3}$$

where I_{xx}, I_{yy}, I_{zz}, I_{xy}, I_{xx}, and I_{xz} are momentum of inertia of the wing. M_{aero}, $M_{elastic}$, and $M_{gravity}$ are the momentum due to aerodynamic, elastic, and gravitational forces, respectively. The aerodynamic forces

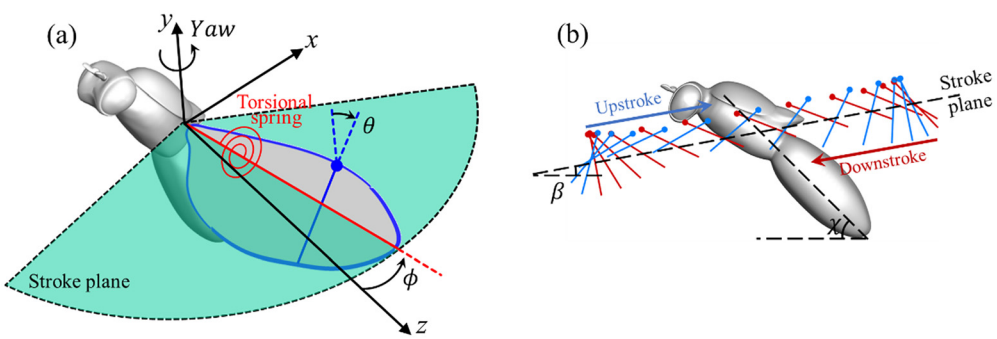

FIG. 2. Schematic of the flapping wing with a torsional spring (a) and wing chord diagram during upstroke and downstroke (b), where θ is the pitch angle, ϕ is the stroke angle, $\beta = 10°$ is the stroke plane angle, and $\chi = 45°$ is the body incline angle.

are obtained by integrating the pressure and shear on the surface of the insect.

The nondimensional torsional stiffness of the wing root is indicated by the Cauchy number (Ch)[50] defined as the ratio of the fluid dynamic pressure force to the structure elastic force, which can be expressed as follows:

$$Ch = \frac{\rho_{air} A_\phi{}^2 f^2 \bar{c}^3 b^2}{G}, \tag{4}$$

where $\bar{c}$ is the mean wing chord length and b is the wing spanwise length. The Cauchy number selected in this paper is 0.27 based on our previous study.[48,51] Both the lift generation and power consumption are optimized at this Cauchy number.

The implicit method used to couple the fluid flow field with the motion of solid wings is briefly introduced here. At each time step, the pressure and viscous forces can be obtained by solving the Navier–Strokes equations. Euler angular accelerations of the wings are updated from the wing torsional spring model, which includes the aerodynamic forces, elastic forces, gravitational forces, and inertia forces. Velocities on the wings are then updated and applied back to the Navier–Stokes solver as boundary conditions to obtain an updated flow field. This two-way coupling process for solving both the fluid dynamic and wing kinematics is iterated until the angular accelerations of the wings reach convergence criteria.

C. Odor advection–diffusion equation

At each time step, based on the velocity field, the odor advection–diffusion equation [Eq. (5)] is then solved to obtain the odor concentration landscape. The odor advection–diffusion equation is discretized using an implicit method [Eq. (6)] with the second order accuracy in space,

$$\frac{\partial C}{\partial t} + u_i \frac{\partial C}{\partial x_i} = D \frac{\partial^2 C}{\partial x_i^2}, \tag{5}$$

$$\frac{C^{n+1} - C^n}{\Delta t} + \frac{\delta C^n U_i^n}{\delta x_i} = D \frac{\delta}{\delta x_i}\left(\frac{\delta C^{n+1}}{\delta x_i}\right), \tag{6}$$

where C is the odor intensity, D is the odor diffusivity, U_i is the face-centered velocity obtained from interpolation of the cell-centered velocity u_i.

The odor advection–diffusion equation is discretized on the same non-body-conforming Cartesian grid as the Navier–Stokes equations solver, as shown in Fig. 1. The differential equation for odor transportation can be written as

$$\begin{aligned} &C_P^{n+1} - D\Delta t\left(a_W C_W^{n+1} + a_E C_E^{n+1} + a_N C_N^{n+1}\right. \\ &\quad \left. + a_S C_S^{n+1} + a_B C_B^{n+1} + a_F C_F^{n+1} + a_P C_P^{n+1}\right) \\ &= C_P^n - \Delta t\left(\frac{C_e^n U_e^n - C_w^n U_w^n}{\Delta x} + \frac{C_n^n U_n^n - C_s^n U_s^n}{\Delta y} + \frac{C_f^n U_f^n - C_b^n U_b^n}{\Delta z}\right), \end{aligned} \tag{7}$$

where the coefficients a_W, a_E, a_N, a_S, a_B, a_F, a_P are calculated by discretizing the diffusion term,

$$\begin{aligned} \frac{\delta}{\delta x_i}\left(\frac{\delta C}{\delta x_i}\right) &= \frac{\frac{C_E - C_P}{\Delta x} - \frac{C_P - C_W}{\Delta x}}{\Delta x} + \frac{\frac{C_N - C_P}{\Delta y} - \frac{C_P - C_S}{\Delta y}}{\Delta y} \\ &\quad + \frac{\frac{C_F - C_P}{\Delta z} - \frac{C_P - C_B}{\Delta z}}{\Delta z}, \\ &= a_E C_E + a_W C_W + a_N C_N + a_S C_S + a_F C_F \\ &\quad + a_B C_B + a_P C_P. \end{aligned} \tag{8}$$

This approach has been applied to investigate the odor plume structure perturbed by canonical pitching-plunging motion[52] and flapping wings of insects.[53]

D. Simulation setup

To investigate both aerodynamic and olfactory functions of flying insects during odor-tracking flight, we placed a fruit fly model into a numerical wind tunnel to mimic the upwind surging motion under different incoming flow speeds. Drawing from existing literature,[54] the fruit fly wing model has a wingspan length (b) of 3.08 mm and wing flapping frequency of 198 Hz. The flapping motion results a mean wingtip velocity of $\bar{U}_{tip} = 3.2$ m/s in flapping flight. We are mimicking the wind tunnel experiments of a tethered fruit fly with incoming flow velocity (U_∞) change from 0.47 to 1.88 m/s. This results in a range of reduced frequency ($k = fb/U_\infty$) from 0.325 to 1.3.

The odorant transport phenomenon is characterized by two nondimensional parameters, Reynolds number (Re) and Schmidt number (Sc). The Reynolds number is defined as $\mathrm{Re} = U_\infty b/\nu$, where the fluid kinematic viscosity is around $\nu = 1.608 \times 10^{-5}$ m^2/s at 300 K. The varying incoming flow velocity (U_∞) leads to a varying Reynolds number (Re) ranges from 90 to 360. The Schmidt number ($\mathrm{Sc} = \nu/D$) is a dimensionless quantity to describe the relative effectiveness of momentum diffusion vs mass diffusion in a fluid. It is defined as the ratio of the kinematic viscosity (ν) of the fluid to the mass diffusivity (D) of the particular odorant being studied. Ethanol, commonly used in investigations of fruit fly odor-tracking behavior,[12] has a mass diffusivity of approximately 1.072×10^{-5} m^2/s at 300 K. This yields a Schmidt number of 1.5, a value employed in the current simulation setup.

The simulations were performed in a non-uniform Cartesian mesh. As shown in Fig. 4, a fruit fly model during forward flight is represented by high-density triangular surface mesh. An odor source in front of the fruit fly releasing odor at constant odor concentration is located 1.5 body length away from the antennae, with a square cross section of 0.36×0.36 body length. On each of the antenna, five virtual odor sampling probes are marked and used to analyze the olfactory perception of the antenna. The computational domain size of the simulation is $30b \times 30b \times 30b$ in terms of mean wingspan length (b). The grid resolution is $320 \times 128 \times 240$. The domain mesh consists of three regions. In the center of the domain, a cuboidal region provides the highest resolution of uniformly distributed Cartesian grids around the insect. Around this dense region, there is a layer of secondary dense region where the grid size expands exponentially. Beyond the secondary dense region, there is a coarse stretched layer where grid size expands rapidly. Boundary conditions on all walls of the computational domain are set as Neumann boundary condition except Dirichlet boundary condition is set on the inlet wall with constant

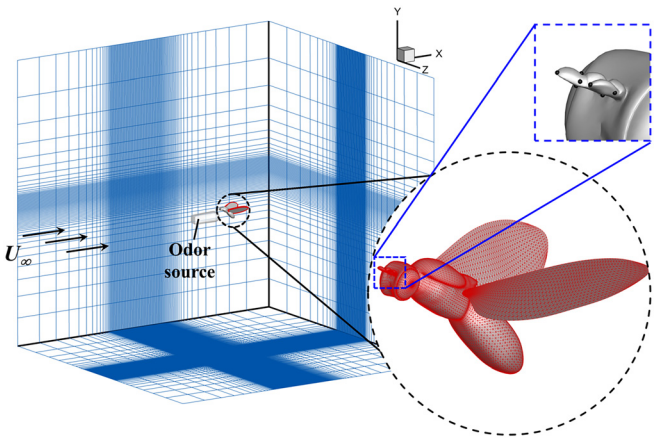

FIG. 4. Simulation setup and computational grids applied in the study. An odor source is placed in front of the fruit fly with a constant odor intensity. On each antenna, there are five virtual probes to sample odor intensity variations during flapping flight. The simulation is performed in a 10×10^6 size non-uniform Cartesian grid. The body and wings are represented by high-density unstructured triangular surface mesh.

incoming velocity and odor intensity. All our simulations were performed for seven flapping cycles to ensure both flow field and odor concentration field reach a periodic state.

The selection of current simulation domain and grid sizes was based on the results of our grids independence study, as shown in Fig. 5. We calculated the time course of lift coefficient C_L using three grid setups, coarse grid, current grid, and fine grid. The time-averaged lift coefficients C_L for the three grid setups are 1.002, 0.989, and 0.983, respectively. By increasing the grid size from 9.83×10^6 (current grid) to 14.42×10^6 (fine grid), there is less than 1% difference for the lift force generated by the flapping wings.

E. Evaluations of aerodynamic and olfactory performance

In Sec. III, the aerodynamic performance will be discussed in terms of force coefficients (lift coefficient C_L and drag coefficient C_D),

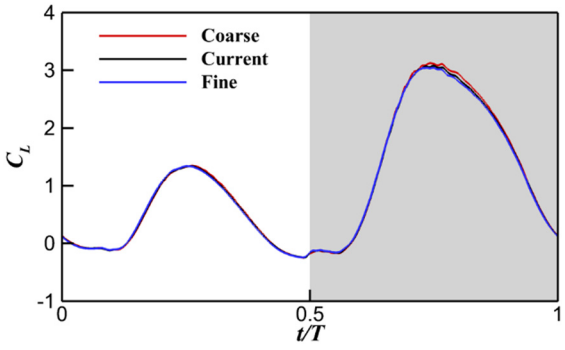

FIG. 5. Comparison of time history of lift coefficient C_L using coarse grid ($288 \times 112 \times 224 = 4.71 \times 10^6$), current grid ($320 \times 128 \times 240 = 9.83 \times 10^6$), and fine grid ($352 \times 160 \times 256 = 14.42 \times 10^6$). The shaded areas represent the downstroke period.

pressure coefficient C_P, and power coefficients (mass specific aerodynamic power P^*_{aero}, mass specific inertial power P^*_{iner}, and mass specific mechanical power P^*_{mech}). Olfaction perception will be presented in terms of normalized odor concentration C^*.

The normalized odor concentration C^* is defined as

$$C^* = \frac{C}{C_0}, \tag{9}$$

where C_0 is the odor concentration at the odor source.

The lift coefficient C_L and drag coefficient C_D are defined as

$$C_L = \frac{F_L}{\frac{1}{2}\rho \bar{U}^2_{tip} S}, \tag{10}$$

$$C_D = \frac{F_D}{\frac{1}{2}\rho \bar{U}^2_{tip} S}, \tag{11}$$

where F_L is the lift force, F_D is the drag force, and S is the wing area.

The aerodynamic power P_{aero} is the power the wing needs to overcome aerodynamic forces, defined as the dot product of aerodynamic forces and velocity,

$$P_{aero} = -\int\int (\Delta P \vec{n} + \Delta \vec{\tau}) \vec{u}\, ds, \tag{12}$$

where ΔP and $\Delta \vec{\tau}$ are the pressure difference between the two sides of the wing surface and shear stress, respectively, $\vec{n}$ is the unit vector normal to the wing, $\vec{u}$ is the velocity on the wing, and s is the area of the wing.

The inertial power P_{iner} is the power needed to overcome inertial force, defined as the dot product of wing inertial force and velocity,

$$P_{iner} = \int\int h\rho_{wing} \frac{d\vec{u}}{dt} \vec{u}\, ds, \tag{13}$$

where h is the wing thickness.

For convenience, the mess specific aerodynamic power $P^*_{aero} = P_{aero}/m$ and inertial power $P^*_{iner} = P_{iner}/m$ are defined as the aerodynamic power and inertial power divided by insect body mess (m), respectively. The mechanical power P^*_{mech} is the summation of P^*_{aero} and P^*_{iner}. Since the torsional spring model is used to calculate passive pitch angle, we assume the wing root is able to store the negative mechanical power.

The pressure in the current study is normalized as pressure coefficient

$$C_P = \frac{P - P_\infty}{\frac{1}{2}\rho U^2_\infty}, \tag{14}$$

where P_∞ is the reference pressure.

To visualize how odor plume transport are affected by the flapping wing kinematics, we plotted streaklines that trace the movement of pseudo odorant particles released upstream, as illustrated in Fig. 6(a). Streaklines essentially represent a continuous stream of particles introduced from an upstream position. Using the Lagrangian tracking method, we determined the trajectories of these particles, providing a visualization of the transport pathways of odor particles released from specific locations. The particle velocities and positions were determined using a 4th odor Runge–Kutta technique. There's a

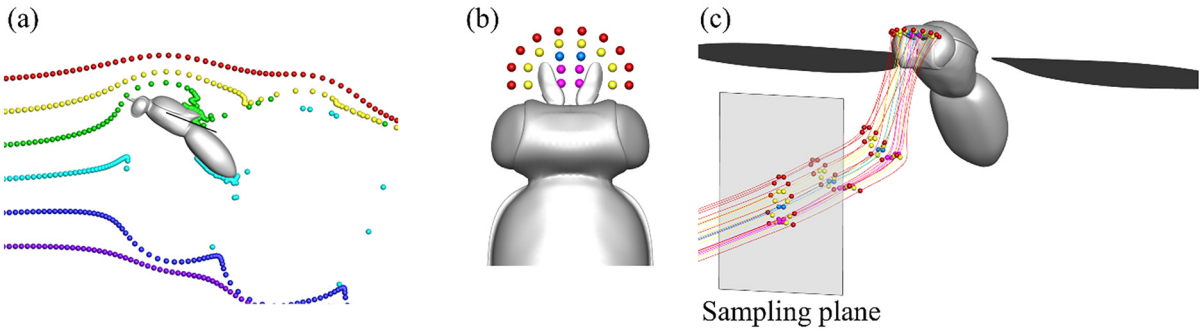

FIG. 6. Schematics illustrating forward and backward Lagrangian tracking approaches. (a) Overview of the forward Lagrangian tracking methodology. (b) Particle release points proximate to the antennae. (c) Computational determination of initial particle locations on the sampling plane via "backward" Lagrangian tracking. The sideview (a) shows streaklines released on the symmetry plane. The backward Lagrangian approach is executed by inverting both time and velocity parameters to trace particle trajectories back to the upstream flow field.

noteworthy similarity between the odor concentration distribution and the streaklines, as both elucidate the odor's structural pattern. However, differences emerge based on the calculation methodologies. While determining odor concentration involves solving for advection in the flow field and diffusion due to concentration gradient, streaklines only factor in the velocity field pertinent to odorant advection, thereby omitting diffusion.

The influence of wing-induced flow on antennal odor concentration is particularly pronounced at elevated levels of reduced frequency. To explore how the antennae interpret the odor plume, we employ a backward Lagrangian tracking methodology, as illustrated in Figs. 6(b) and 6(c). Initially, particles are released in close proximity to the antennae, as depicted in Fig. 6(b). Leveraging the archived instantaneous velocity field and by inversely manipulating both time and velocity variables, we can trace these particles back to their origins in the upstream flow field. Throughout this process, particle velocity and position are interpolated and computed using a 4th order Runge–Kutta method.

III. RESULTS

In this section, we carried out numerical simulations to investigate the aerodynamic performance and odorant dispersion characteristics of a fruit fly model in forward flight. The odor source was positioned upstream and characterized by a Schmidt number (Sc) of 1.5. Our study focused on elucidating the effects of two key parameters: the reduced frequency (k) and the Reynolds number (Re) on the distribution of odorants around the insect and its subsequent odor perception during upwind surging odor-tracking flight. In Subsec. III A, we presented the findings for a baseline scenario, where $k = 0.65$ and $Re = 180$. Subsection III B delves into the influence of varying reduced frequencies (k), ranging from 0.325 to 1.3. This was accomplished by modifying the velocity of the incoming air. Finally, Subsec. III C examines the effects of changing the Reynolds number by altering the kinematic viscosity (ν), while keeping the Schmidt number constant. To ensure the simulations reach a periodic state, all simulations are carried out over a duration of seven flapping cycles.

A. Baseline case

The transport of odorants is fundamentally characterized by two dimensionless parameters: the Reynolds number (Re) and the Schmidt number (Sc). In the baseline scenario, the Reynolds number is set at 180. Ethanol, a commonly employed odorant in prior experiments involving fruit flies,[12] dictates a Schmidt number of 1.5 for ethanol in air, which is adopted for the baseline case. As for the flapping wing kinematics in the fruit fly model, only the leading-edge motion is prescribed. The wing's pitch motion is determined through a torsional spring model, which is integrated with a Navier–Stokes-based CFD solver using a two-way coupling method. In this baseline case, the reduced frequency is set at 0.65, corresponding to a forward flying speed of 0.94 m/s for the fruit fly.

Figure 7 provides a temporal analysis of aerodynamic performance for the baseline case, focusing on force coefficients, passive wing pitch angle, and mass-specific power consumption during the 6th and 7th flapping cycles. In this forward flight configuration, the wing's stroke plane is inclined at an angle of 10 deg relative to the horizontal plane. This inclination results in asymmetric wing kinematics between the upstrokes and downstrokes, thereby creating significant disparities in aerodynamic forces and power consumption for each. The time-averaged lift coefficient for this scenario is 0.989, with downstrokes contributing to 79% of the total lift generated. As shown in Fig. 7(b), the time-averaged drag coefficient stands at −0.0192, confirming that the current setup closely mimics the cruising flight behavior of a fruit fly. Figure 7(c) outlines the temporal evolution of the calculated passive pitching angle, defined as the angle between the wing and the vertical axis. Due to the angle of the stroke plane and the incoming air velocity, the average pitch angle during the downstroke (55.7°) is markedly greater than that during the upstroke (−28.2°). To offer a more holistic view of passive wing pitch kinematics, Fig. 8 illustrates transient wing chord positions and corresponding aerodynamic forces over the course of a single stroke cycle. As anticipated, the bulk of the aerodynamic force is generated during mid-downstroke, with minimal force manifesting during wing reversal.

Figure 7(d) illustrates the temporal evolution of mass-specific aerodynamic power, inertial power, and mechanical power, all of which are normalized by the insect's total body mass. The graph reveals that inertial power fluctuates between positive and negative values within a single stroke cycle. It rises initially due to wing acceleration at the commencement of each stroke—whether downstroke or upstroke—and subsequently changes sign as the wing decelerates toward the end of the stroke. In contrast, the aerodynamic power

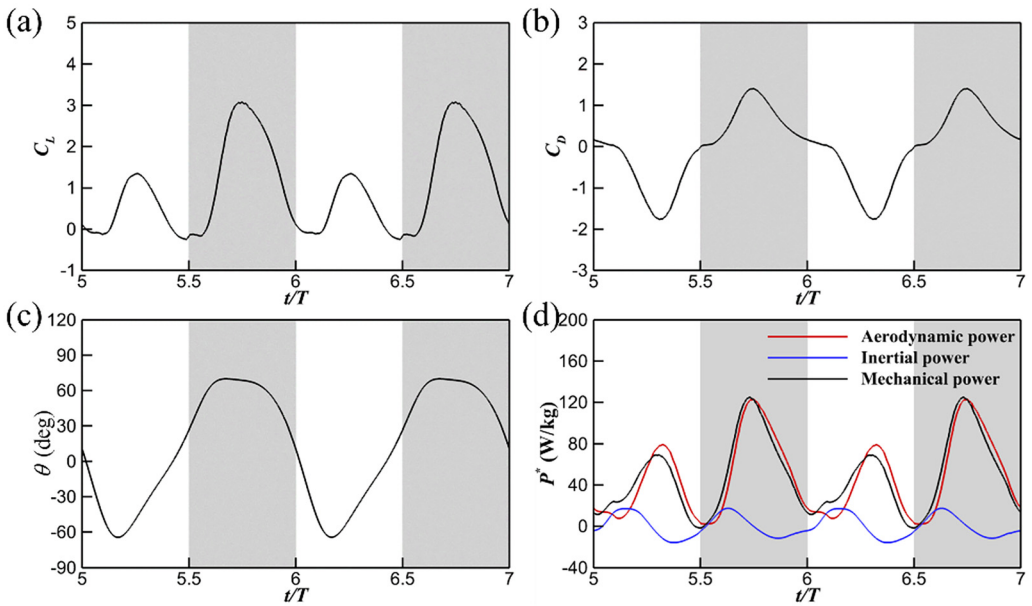

FIG. 7. Time history of lift coefficient C_L (a), drag coefficient C_D (b), wing pitch angle θ (c), and mass specific power P^* (d) for the baseline case. The mechanical power in (d) is the summation of the mass specific aerodynamic power and inertial power. The shaded areas represent the downstroke period.

remains positive throughout the stroke cycle, albeit modest near the stroke reversals. Its fluctuating pattern closely mirrors that of aerodynamic forces. During downstrokes, aerodynamic power is dominant and peaks around mid-downstroke. Conversely, aerodynamic power during upstrokes is significantly lower, reaching its apex around mid-upstroke. Mechanical power, representing the sum of both inertial and aerodynamic components over the flapping cycles, has a cycle-averaged mass-specific value of 48.6 W/kg. Of this, downstrokes account for 64% of the power, which is somewhat greater than values reported for hovering fruit flies. Upon recalculating data from Ref. 55 based on our definitions, the mass-specific mechanical power for hovering fruit flies is approximately 29.1 W/kg with zero elastic energy storage and 34.5 W/kg with full energy storage. This elevated power consumption is expected since forward flight requires not only sufficient lift to counteract gravity but also adequate thrust to overcome air resistance.

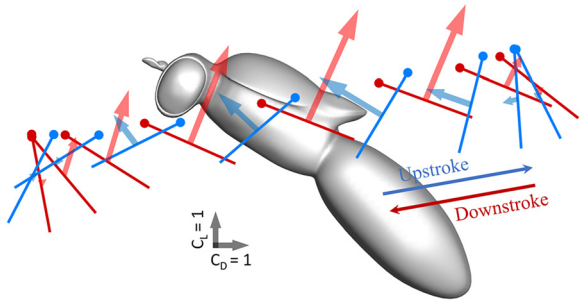

FIG. 8. Wing chord diagram for the baseline case. The circles and lines denote wing leading edges and mid wing chords, respectively. The red and blue color represent the duration of downstroke and upstroke, respectively. The arrows attached on the wing chord denote the strength and direction of the net aerodynamic forces generated by the wing. The time interval between each wing chord is $\Delta t/T = 0.0625$.

To gain deeper insights into the flow field, we employ the Q-criterion to visualize the wake structure. Figure 9 presents four snapshots during flapping motion featuring both side and top views of the wake topology, which are color-coded by the pressure coefficient. During the downstroke, the flapping wings generate pronounced leading-edge and tip vortices, which subsequently shed into the flow field. These vortices work in concert with the downwash flow to provide majority of lift, essential for supporting the insect's body weight. In contrast, the vortices produced during the upstroke are significantly weaker. The periodically shed vortices coalesce to form a succession of vortex rings in the wake.

To assess how the fruit fly detects an odor plume, we measured the odor concentration at five specific locations on each antenna, indicative of the insect's olfactory sensitivity, as depicted in Figs. 10(a) and 10(b). Figure 10(c) presents the temporal variations in odor concentration at these points. Olfactory sensitivity is strongly correlated with the position of these sampling points. At the tip of the antenna (point 1, represented in red), the concentration is highest, as it is oriented directly toward the odor source. Concentration levels at the rear (point 2, yellow) and inner (point 4, blue) points consistently exceed those at the front (point 3, green) and outer (point 5, pink) points. Under the conditions of the current simulation, all five points exhibit similar trends: olfactory sensitivity peaks during the upstroke and reaches its nadir during the downstroke. To simplify the analysis, we use the average concentration value across these five points to represent overall antenna sensitivity in subsequent sections. This trend can be elucidated by cross-sectional side views of odor concentration, as shown in Figs. 11(a1)–11(d1). Generally, the wing-induced airflow

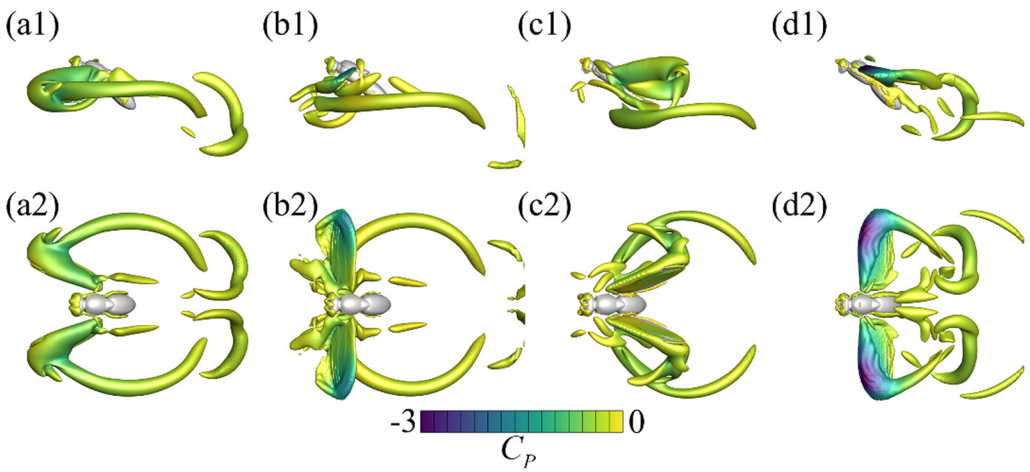

FIG. 9. Wake topology visualized by plotting iso-surface of Q-criterion from side and top views, respectively, at t/T = 0 (a1), (a2), 0.25 (b1), (b2), 0.5 (c1), (c2), 0.75 (d1), (d2) for the baseline case. The wake topologies are color coded by pressure coefficient C_p.

generates a "saddle point" near the thorax, which lifts the odor plume above the antenna region during downstrokes and draws it downward during upstrokes (Fig. 13).

To underscore the influence of wing flapping on odor detection, we also conducted a 'body-only' simulation, holding all parameters constant except for removing the wings from the fruit fly model. As illustrated in Fig. 12, the absence of wing flapping prevents the upward induction of the odor plume toward the antennas, resulting in significantly reduced olfactory sensitivity, as indicated by the black dashed line in Fig. 10(c).

To explore the impact of wing-flapping kinematics on odor plume transport, Fig. 11 provides side and top views of odor concentration cross sections and streaklines. The flapping wing kinematics dramatically alter the odor landscape surrounding the insect, primarily directing the odor plume upward. During the upstroke phase (t/T = 0–0.5), wing-induced airflow pulls the odor plume downward toward the antennae, resulting in heightened olfactory sensitivity. Conversely, during the downstroke phase (t/T = 0.5–1), wing flapping generates a strong induced flow near the thoracic region that propels the odor plume upward, away from the antennae, diminishing

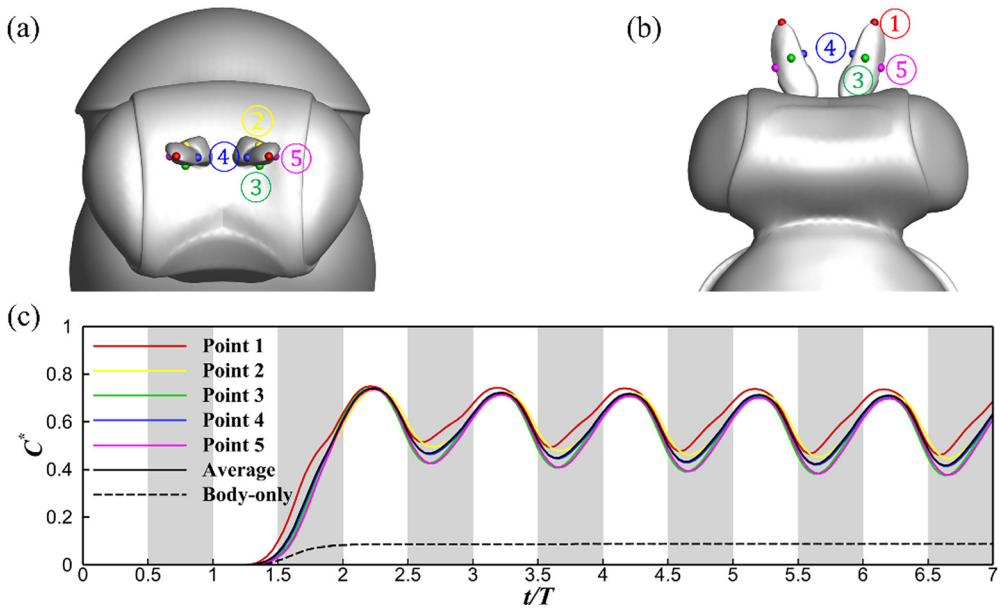

FIG. 10. Five odor sampling points on each antenna shown in top view (a) and front view (b). Time history of the normalized odor concentration C^* on the five sampling points on the left antenna for the baseline case and the average for the baseline and body-only case (c).

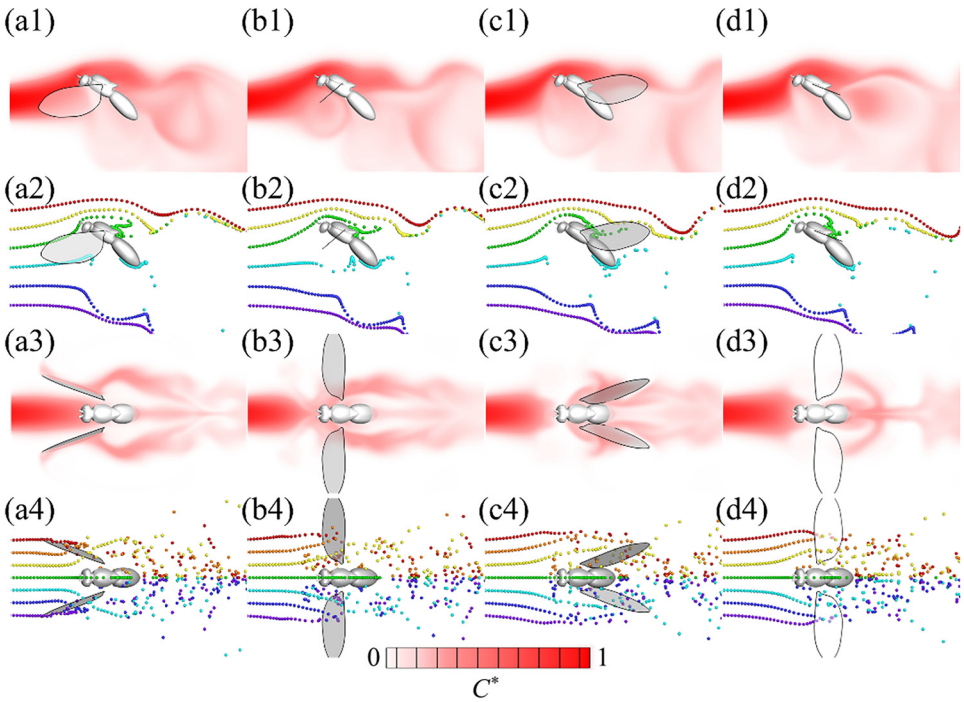

FIG. 11. Odor concentration field (first and third rows) and streaklines (second and fourth rows) for the baseline case at four key instants during a flapping cycle: $t/T = 0$ (a1)–(a4), 0.25 (b1)–(b4), 0.5 (c1)–(c4), and 0.75 (d1)–(d4), during a flapping cycle. The upper two rows display the data on the symmetry plane from a lateral perspective, while the lower two rows offer a top–down view.

olfactory sensitivity. This phenomenon aligns with what has been previously termed the "trap-and-flick" mechanism.[23] Throughout a complete stroke cycle, several streamlines, disturbed by unsteady flow, intersect the antennal region, expanding the range of odor detection.

For comparison, Fig. 12 displays the side and top views of odor concentration cross sections and streaklines in a wingless ("body-only") scenario. In the absence of wing flapping, the odor plume struggles to reach the antennae. Interestingly, as revealed in the top-view streaklines [Figs. 11(a4)–11(d4)], only a narrow jet of odorant particles (depicted in green) in the lateral direction successfully navigates through the antennae. Particles emanating from other locations, although affected by wing flapping, are largely undetected by the antennae.

In Figs. 11(a1)–11(d1), the odor concentration contours reveal a region of low odor concentration situated beneath the insect's thorax. Corresponding streaklines, depicted in cyan in Figs. 11(a2)–11(d2), curve downward. To elucidate this phenomenon, Fig. 13 presents the time-averaged velocity contours superimposed with streamlines for the baseline case. A velocity-null saddle point emerges just anterior to the thorax where both flapping wings meet. This saddle point acts as a nexus, drawing odorants from a broad spatial extent due to the wing-induced airflow. At this point, lateral velocities from each wing effectively cancel each other out due to the symmetrical flapping kinematics, while streamwise velocities are also nullified by opposing wing-induced flows. As shown in Fig. 13(b), this saddle point bifurcates the streamlines into two distinct pathways: one channeling upward over the insect and the other steering downward beneath it. Consequently, the odorants detected by the antennae are a mix of those advected from the saddle point by wing-induced flows and those coming directly from upstream regions.

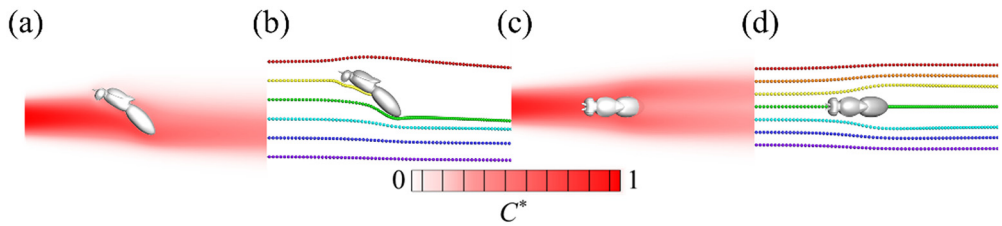

FIG. 12. Odor concentration field (a), (c) and streaklines (b), (d) for the body-only case when the flow field reached to a steady state. The data are presented from both side view (a), (b) on the symmetry plane and top view (c), (d), respectively.

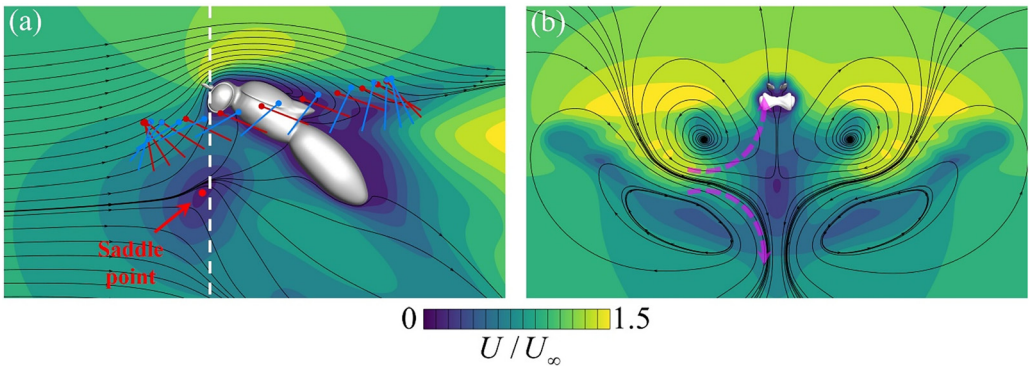

FIG. 13. Time-averaged velocity field overlaid with streamlines for the baseline case: side view (a) on the symmetry plane and top view (b). A point in figure (a) exhibiting zero velocity is identified as a saddle point, as the surrounding velocity contour form a saddle-like shape. The white dashed line in figure (a) indicates the location of the vertical cross-sectional plane displayed in figure (b).

B. Effects of reduced frequency

Fruit flies exhibit a range of flight speeds when seeking out odor plumes emanating from objects of interest. This section explores the impact of forward flight velocity on both the structure of the odor plume and the sensitivity of the antennae to these odors. We scrutinize the effects of varying forward flight velocities in terms of the reduced frequency, denoted as $k = fb/U_\infty$, within the span of 0.325–1.3. This translates to an actual velocity range of 0.47–1.88 m/s. Aside from adjustments to the reduced frequency, all other simulation parameters remain consistent with the baseline case.

Figure 14 shows the time history of aerodynamic force coefficients, mass specific power consumption, and passive wing pitch angle at different k value. The time-averaged $\bar{C}_L$, $\bar{C}_D$, $\bar{\theta}$, and $\bar{P}^*_{mech}$ during upstroke, downstroke, and an entire stroke cycle are summarized in Table I. Note that smaller k indicates larger forward velocity. As k increases, we see that the flapping wings generate larger aerodynamic forces (lift and drag) and consume more power during upstroke. While during downstroke, the wings generate smaller aerodynamic forces and consume less power. The cycle-averaged $\bar{C}_L$ decrease with k. As for the drag, since we kept the same stroke plane angle for all the

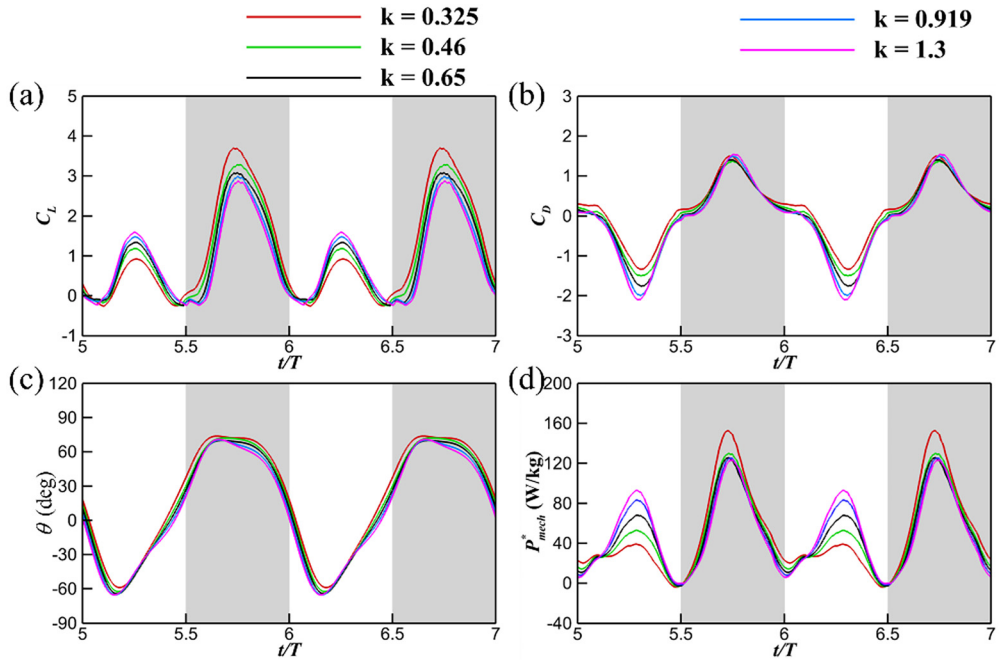

FIG. 14. Time history of lift coefficient C_L (a), drag coefficient C_D (b), pitch angle θ (c), and mass specific mechanical power P^*_{mech} (d) for cases with different reduced frequency (k) ranging from 0.325 to 1.3.

TABLE I. Summary of time-averaged lift coefficient $\bar{C}_L$, drag coefficient $\bar{C}_D$, wing pitch angle $\bar{\theta}$, and mass specific power $\bar{P}^*_{mech}$ for cases with different reduced frequency (k) during upstroke, downstroke, and an entire flapping cycle.

	Upstroke				Downstroke				Cycle-average			
k	$\bar{C}_L$	$\bar{C}_D$	$\bar{\theta}$ (deg)	$\bar{P}^*_{mech}$ (W/kg)	$\bar{C}_L$	$\bar{C}_D$	$\bar{\theta}$ (deg)	$\bar{P}^*_{mech}$ (W/kg)	$\bar{C}_L$	$\bar{C}_D$	$\bar{\theta}$ (deg)	$\bar{P}^*_{mech}$ (W/kg)
0.325	0.238	−0.410	−21.8	23.30	2.027	0.719	61.7	76.43	1.132	0.155	20.0	49.84
0.46	0.349	−0.578	−26.0	28.98	1.751	0.664	58.1	67.06	1.049	0.043	16.1	47.99
0.65	0.424	−0.688	−28.2	34.66	1.557	0.649	55.7	62.74	0.990	−0.019	13.8	48.66
0.919	0.493	−0.766	−30.0	39.83	1.381	0.638	53.4	59.74	0.936	−0.064	11.7	49.74
1.3	0.548	−0.808	−31.6	43.32	1.260	0.635	51.8	57.76	0.903	−0.087	10.1	50.49

cases, at smaller k (larger forward velocity), the flapping wings generate positive drag force. At larger k (smaller forward velocity), the flapping wings generate nagetive drag force (thrust). The pitch angle θ is calculated using the torsional spring model elaborated in Sec. II B which includes the aerodynamic forces, elastic forces, gravitational forces, and momentum forces acted on the wing. Since the aerodynamic force is smaller at larger k, the cycle-averaged pitch angle $\bar{\theta}$ also decreases with k. In summary, both the cycle-averaged aerodynamic forces and passive wing pitch angles exhibit a decreasing trend with rising reduced frequency.

Figure 15 presents the wake topology colored by pressure coefficient C_P for different k at mid-downstroke. At smaller k, the larger incoming air velocity generates stronger wingtip vortex and trailing edge vortex that shed downstream. As k increases, the strength and size of wingtip vortex and trailing edge vortex decrease, while the vortices shed during upstroke are larger in size. Concurrently, these wingtip and trailing-edge vortices, along with those generated during upstrokes, coalesce to form a chain of interconnected vortex rings.

Figure 16 displays the variations in antennal odor sensitivity across different values of the reduced frequency (k). Within the current simulation setup, we observe that lower k values (0.325–0.65), corresponding to higher forward velocities, result in heightened odor sensitivity on the antennae. Conversely, higher k values (0.919–1.3) yield markedly reduced odor sensitivity. Interestingly, lower k values maximize odor sensitivity during upstrokes and minimize it during downstrokes, a trend that is inverted at higher k values.

To clarify this phenomenon, we refer to Fig. 17, which showcases time-averaged velocities normalized by the incoming air velocity (U/U_∞). Here, higher U/U_∞ values indicate stronger wing-induced flows. At $k = 0.325$ [Figs. 17(a1) and 17(a2)], the incoming air velocity is the largest such that no saddle point is formed before the thorax. The wing-induced flow in this case can hardly affect the flow field near the antennae. However, when k rises to 0.65 (the baseline case), wing-induced flow establishes a saddle point anterior to the insect's thorax. Several streamlines are deviated upward to the antennae region and the normalized air velocity around the antennae is greatly increased. At $k = 1.3$, wing-induced flow is most pronounced, leading to both a saddle point and an isolated stagnation point ahead of the thorax. Streamlines between these two points form a shield-like airflow over the insect, essentially enclosing the antennae. Consequently, the antennae primarily detect odors funneled to the stagnation point by the wings, rather than those advecting from upstream. This flow characteristic largely accounts for the substantially lower odor concentrations observed at high k values (0.919–1.3) as shown in Fig. 16.

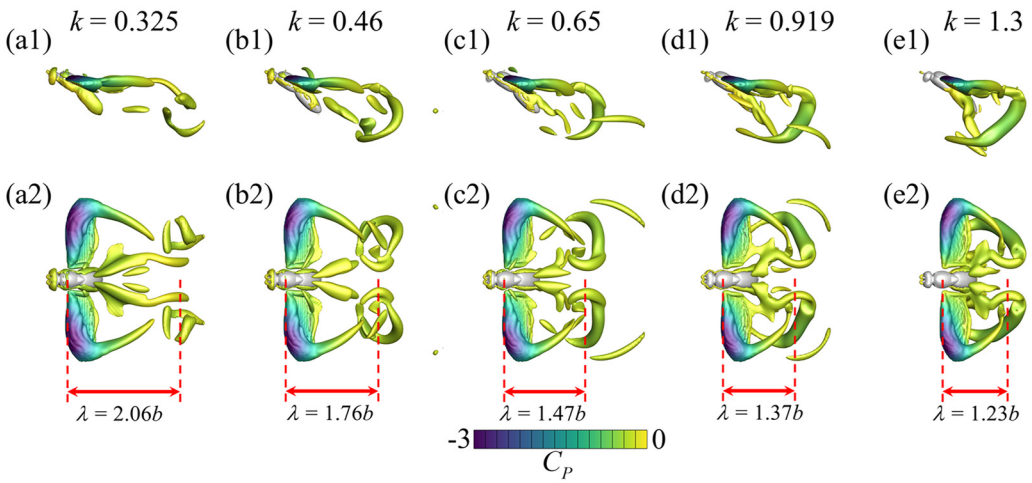

FIG. 15. Wake topology visualized by plotting iso-surface of Q-criterion from side and top views at mid-downstroke ($t/T = 0.75$) for the cases with different reduced frequency $k = 0.325$ (a1), (a2), 0.46 (b1), (b2), 0.65 (c1), (c2), 0.919 (d1), (d2), and 1.3 (e1), (e2). The wake topologies are color coded by pressure coefficient C_p.

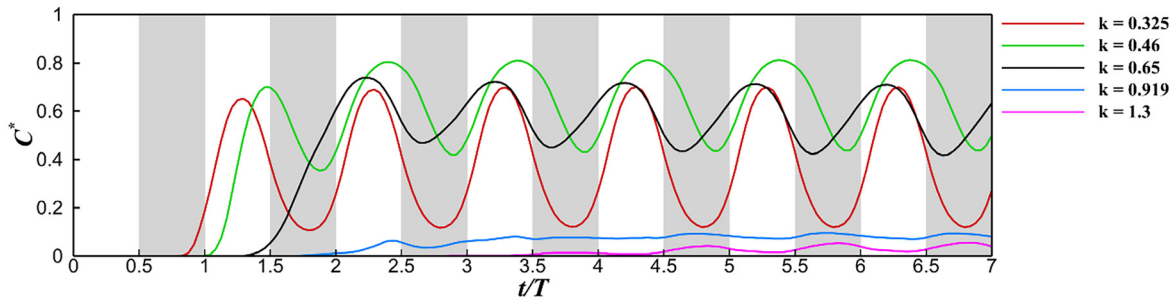

FIG. 16. Time history of the normalized odor concentration C^* for cases with different reduced frequency (k) ranging from 0.325 to 1.3.

Figure 18(a) shows the time-averaged normalized odor concentration C^* on the antennae for different k. In which the fruit flies are colored by odor concentration to provide a comprehensive understanding of odor perception of the insects. Under current setup, at $k = 0.46$, the odor sensitivity on the antennae reaches to its maximum. As k continues to increase, the odor sensitivity decreases. Since the odor sensitivity is greatly affected by the wing-induced flow, we present the cycle-averaged velocity magnitude near the antennae normalized by incoming air velocity in Fig. 18(b) as an indicator of the strength of wing-induced flow. From the normalized air velocity contour U/U_∞, we see that the intensity of wing-induced flow increases with k. At $k = 0.65$, a saddle point occurs before the thorax and greatly alters the flow field around the antennae. As k continues to increase ($k = 0.919$ and 1.3), the wing-induced flow becomes increasingly dominant in the antennae region, such that a stagnation point in addition to the saddle point occurs before the thorax. At the antennae region, the normalized velocity increases, and the odor concentration is significantly reduced.

Figure 19 displays both side and top views of the normalized odor concentration contours and streaklines at a reduced frequency $k = 0.325$, a condition where the incoming airflow primarily dominates the flow dynamics. Under these conditions, the odor plume in the vicinity of the antennae is minimally disturbed by wing-induced flows. Notably, the wing-induced flow is more potent during the downstroke phase ($t/T = 0.5$–1), causing an upward deflection of the odor plume. This allows the plume to reach the antennae by mid-upstroke, as seen in Fig. 19(b1). Conversely, the plume is drawn downward at mid-downstroke [Fig. 19(d1)] due to the wing-induced flow generated during the upstroke ($t/T = 0$–0.5). As a result, odor sensitivity is maximized during the upstroke and minimized during the downstroke.

Figure 20 offers corresponding visualizations for $k = 1.3$, a setting where wing-induced flow predominantly shapes the airflow surrounding the antennae. During the upstroke, Fig. 20(b1) reveals an odor filament forming at a stagnation point anterior to the thorax, reaching the antennae by mid-downstroke [Fig. 19(d1)]. As previously discussed in Fig. 17(c1), this particular odor plume is conveyed by the wing-induced flow to the stagnation point before being advected to the antennae. Thus, at $k = 1.3$, odor sensitivity is maximized during downstroke and minimized during upstroke.

Across all examined reduced frequencies, not only is a high-velocity region situated around the antennae (as shown in Fig. 17), but the odor concentration there is also significantly higher than in other parts of the insect body [Fig. 18(a)]. This observation provides further

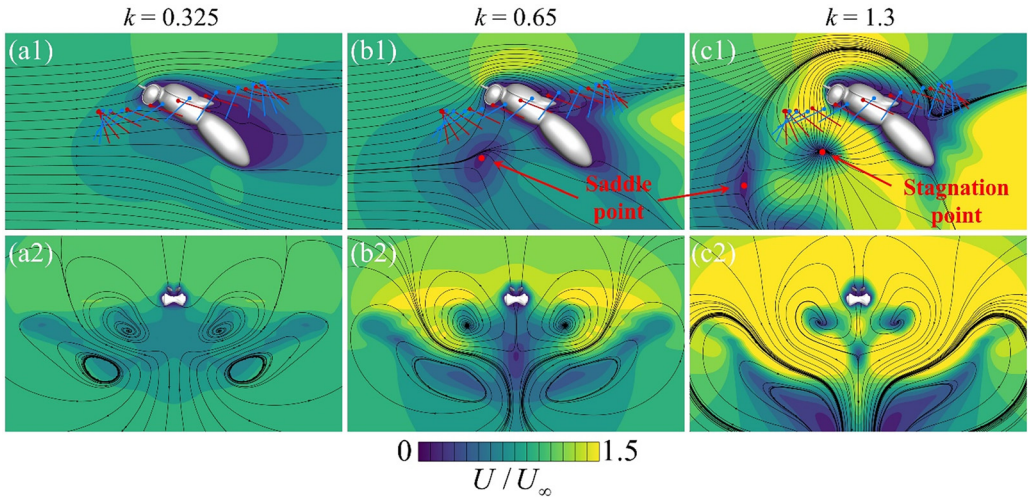

FIG. 17. Time-averaged velocity field overlaid with streamlines for $k = 0.325$ (a1), (a2), $k = 0.65$ (b1), (b2), and $k = 1.3$ (c1), (c2). The sideviews (a1)–(c1) show data on the symmetry plane.

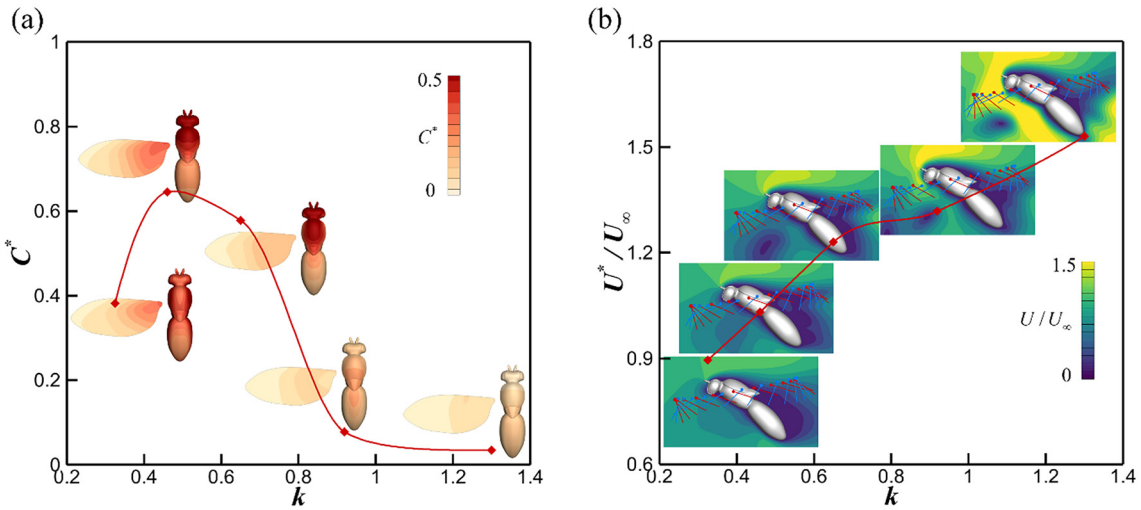

FIG. 18. Time-averaged normalized odor concentration C^* on the antennae (a) and cycle-averaged velocity magnitude on the symmetry plane near the antennae normalized by incoming air velocity U^*/U_∞ (b) for different k. The fruit flies colored by C^* for different k are shown in (a).

evidence that the antennae are strategically positioned for optimal odorant detection. In contrast, for other body regions, such as the dorsal area, high odor concentrations [Fig. 18(a)] may exist, but the reduced air velocity and increased distance could delay the timing of odor perception, thereby compromising the temporal resolution of odor detection.

To further explore the impact of different reduced frequencies k on the range of odor sampling, we employed a backward Lagrangian

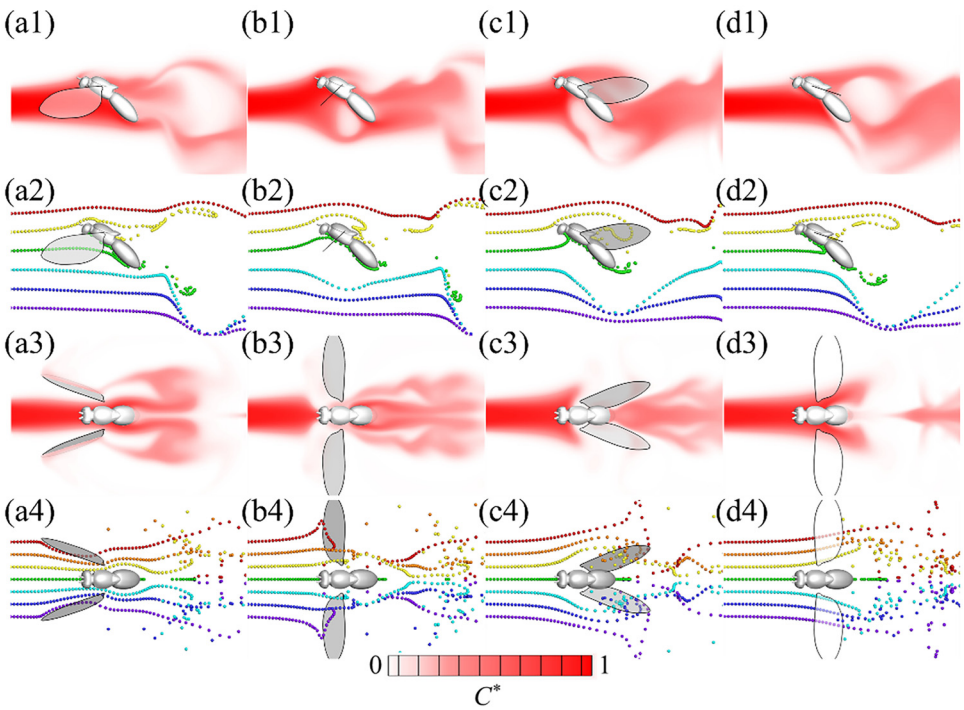

FIG. 19. Odor concentration field (first and third rows) and streaklines (second and fourth rows) for the k = 0.325 case at four key instants during a flapping cycle: t/T = 0 (a1)–(a4), 0.25 (b1)–(b4), 0.5 (c1)–(c4), and 0.75 (d1)–(d4), during a flapping cycle. The upper two rows display the data on the symmetry plane from a lateral perspective, while the lower two rows offer a top–down view.

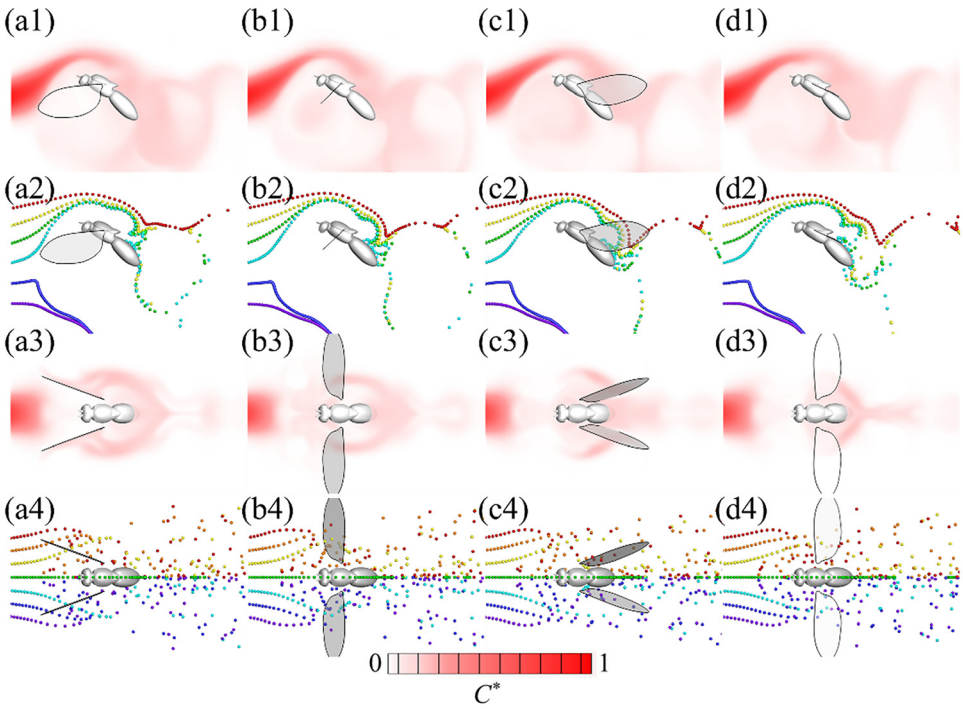

FIG. 20. Odor concentration field (first and third rows) and streaklines (second and fourth rows) for the $k = 1.3$ case at four key instants during a flapping cycle: t/T = 0 (a1)–(a4), 0.25 (b1)–(b4), 0.5 (c1)–(c4), and 0.75 (d1)–(d4), during a flapping cycle. The upper two rows display the data on the symmetry plane from a lateral perspective, while the lower two rows offer a top–down view.

tracking approach. This allowed us to trace the initial locations from which odor particles are released and can eventually reach the antennae to be sensed by the insect. We first released particles continuously in the vicinity of the antennae and used the stored instantaneous data to track the particles backward into the upstream flow field. As illustrated in Fig. 21, initial locations are calculated and corresponding odor intensity index lines are plotted for varying k values.

For smaller k values, as shown in Fig. 21(a), the odor sampling range primarily centers in front of the antennae. As k increases, wing-induced flow begins to dominate the flow field. As a consequence, the regions of odor sampling shift downward but remain centered near the symmetry plane, as seen in Figs. 21(b) and 21(c). At $k = 0.919$ and 1.3 [Figs. 21(d) and 21(e)], the initial locations for odorant particles disperse more broadly across the sampling plane, yet the region of high odor concentration is positioned even lower. Notably, few initial points in these cases lie near the symmetry plane, suggesting that the antennae can sense odors from a considerably wider area.

Figure 22 summarizes the changes in odor sampling regions corresponding to different k values. As k increases, the sampling boundary not only moves downward but also expands in area. This is due to the

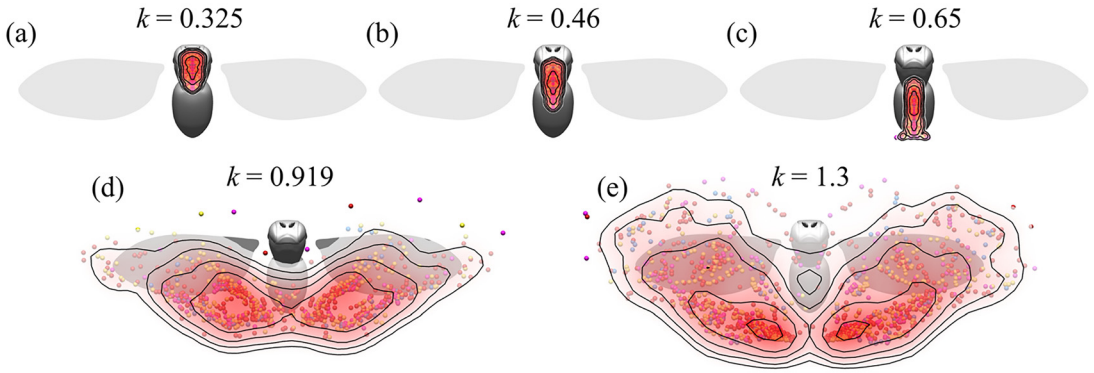

FIG. 21. Schematics illustrating odor sampling range calculated using backward Lagrangian tracking approaches for the cases with different reduced frequency: $k = 0.325$ (a), 0.46 (b), 0.625 (c), 0.919 (d), and 1.3 (e).

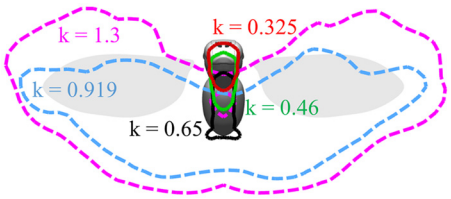

FIG. 22. Comparison of odor sampling range for the cases with different reduced frequency (k).

diminishing incoming velocity and the increasing dominance of wing-induced flows around the insect. As a result, a larger area of odorant particles can be drawn toward the antennae, thereby expanding the insect's perception range of odor plumes. However, this perception range is still relatively limited when compared to the territory navigated during odor-tracking flights. Insects may still employ zigzagging motions to actively enhance their odor-sampling range. Upon detecting an odor plume, the insects are likely to adopt a higher velocity (lower k) during upwind surges, enhancing their odor sensitivity and aiding them in locating the odor source. These findings could elucidate two distinct behaviors observed in insects during odor-guided flights: zigzagging crosswind at lower velocities when searching for odor plumes and surging upwind at higher velocities upon detecting an odor plume.

C. Effects of Reynolds number

Figure 23 illustrates the temporal evolution of aerodynamic performance and passive wing pitch angle for a fruit fly at varying Reynolds numbers. In the range between $Re = 90$ and $Re = 360$, we observe only minimal changes in passive wing pitch angles. This suggests that viscous forces have a negligible effect on the fluid–structure interaction of the passively pitching wing. As Re increases, the lift force exhibits a modest uptick, peaking at the midpoint of the downstroke. Due to pronounced viscous effects at lower Re, elevated drag forces are generated during forward flight, resulting in higher overall power consumption, as depicted in Fig. 23(d).

Figure 24 reveals the wake topology, colored by the pressure coefficient, at $Re = 90$, $Re = 180$, and $Re = 360$ during mid-downstroke. At $Re = 90$, viscous diffusion predominates, causing rapid dissipation of kinematic energy into the surrounding air. At $Re = 180$, two vortex rings composed of several smaller vortices are shed into the downwash flow. At $Re = 360$, these vortex rings are considerably larger than in the other cases and travel greater distances with the downwash. This behavior is likely due to the larger Re values inhibiting the dissipation of the vortices, thereby generating elongated, interconnected vortex rings.

Significant variations in odor sensitivity across different Reynolds numbers (Re) are evident from Fig. 25. As Re rises, there is a corresponding increase in both the magnitude and amplitude of odor sensitivity. To elucidate this phenomenon, Fig. 26 presents the time-averaged velocity field near the antennae, normalized using the incoming air velocity, for $Re = 90$, $Re = 180$, and $Re = 360$. The velocity field displays an ascending trend with increasing Re, which likely contributes to the heightened odor sensitivity. Specifically, at $Re = 360$ [as shown in Fig. 26(c2)], the saddle point shifts downward and the streamlines become asymmetrical. The contribution of odor diffusivity (D) to these changes in odor sensitivity becomes more apparent when examining Figs. 27 and 28, which present the normalized odor

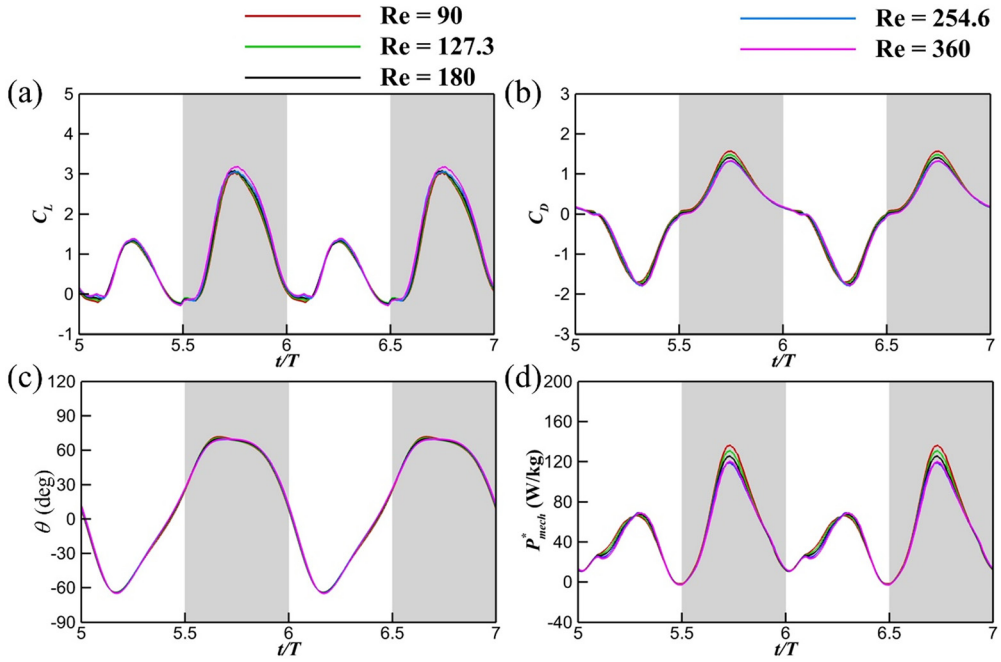

FIG. 23. Time history of lift coefficient C_L (a), drag coefficient C_D (b), pitch angle θ (c), and mass specific mechanical power P^*_{mech} (d) for cases with different Reynolds number (Re) ranging from 90 to 360.

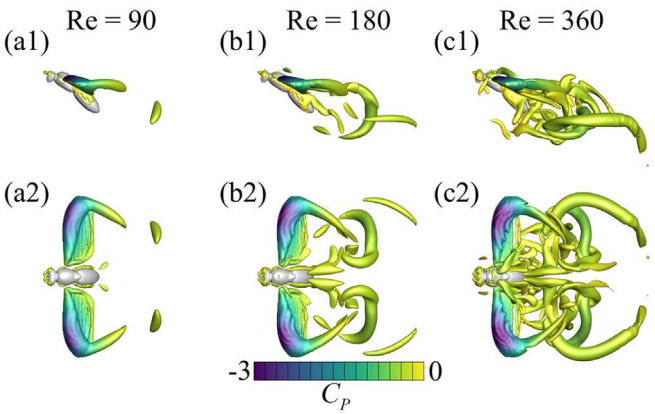

FIG. 24. Wake topology visualized by plotting iso-surface of Q-criterion from side and top views at mid-downstroke ($t/T = 0.75$) for the cases with different Reynolds number $Re = 90$ (a1), (a2), 180 (b1), (b2), and 360 (c1), (c2). The wake topologies are color coded by pressure coefficient C_p.

concentration contour and streaklines for various *Re*. At lower *Re* values (as depicted in Fig. 27), *D* is substantial, and thus, diffusivity is the predominant factor governing odor transport. Consequently, the odor structure is less distinguishable, and the odor concentration at the posterior of the fruit fly model is notably reduced, as revealed in Fig. 29(a). In contrast, at higher *Re* (illustrated in Fig. 28), *D* is considerably smaller, and advection becomes the dominant mechanism for odor transport. The odor plume structure is much more well-defined and resembles streaklines, resulting in the highest odor concentration at the rear of the fruit fly model among all cases examined, as indicated in Fig. 29.

IV. CONCLUSIONS

In this study, we have explored the intricate relationship between aerodynamics and olfaction in the odor-tracking flight of fruit flies, extending across a broad range of reduced frequencies and Reynolds numbers. The instantaneous flow field and odor landscape are obtained by solving the three-dimensional Navier–Stokes equations, coupled with equations of motion for the passive pitching wings, and the advection–diffusion equation for the odor transport.

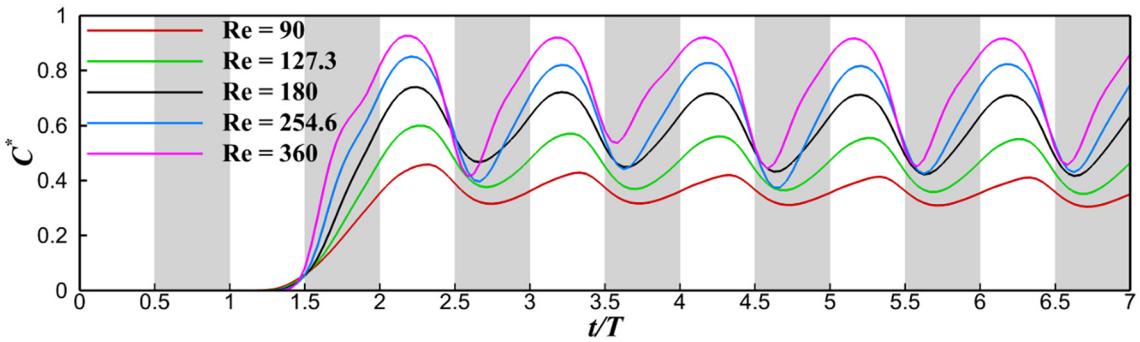

FIG. 25. Time history of the normalized odor concentration C^* for cases with different Reynolds number (*Re*) ranging from 90 to 360.

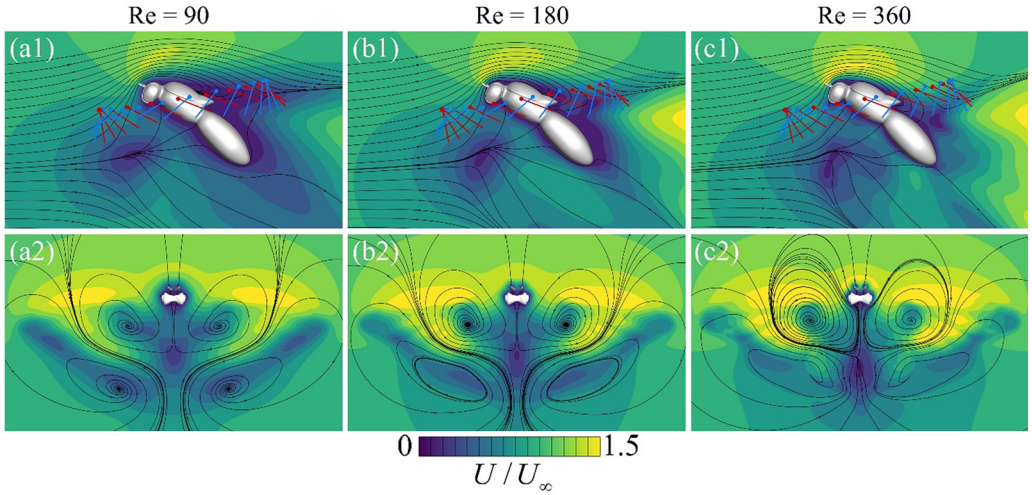

FIG. 26. Time-averaged velocity field overlaid with streamlines for $Re = 90$ (a1), (a2), $Re = 180$ (b1), (b2), and $Re = 360$ (c1), (c2). The sideviews (a1)–(c1) show data on the symmetry plane.

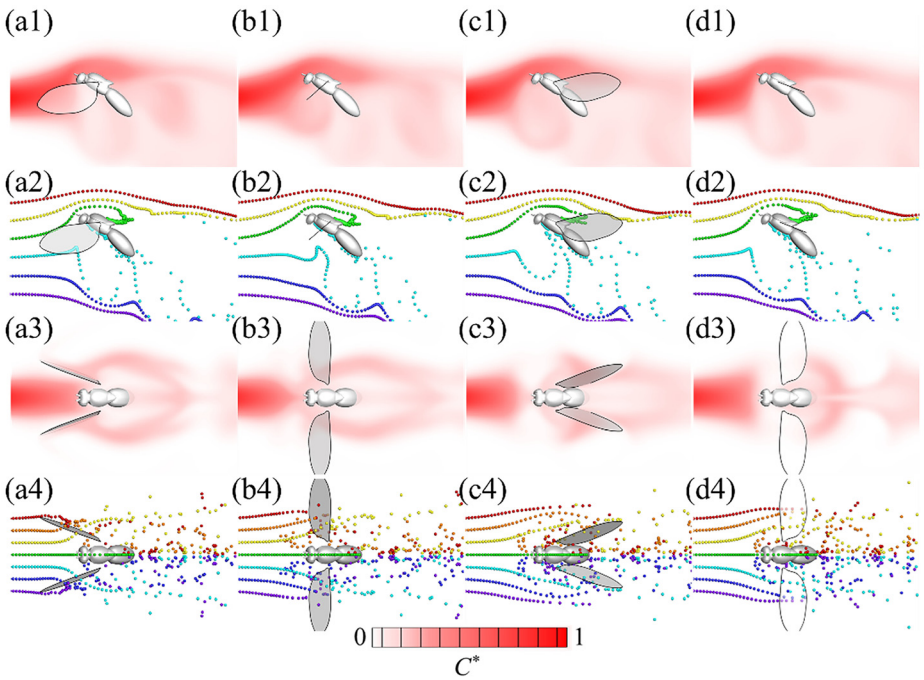

FIG. 27. Odor concentration field (first and third rows) and streaklines (second and fourth rows) for the $Re = 90$ case at four key instants during a flapping cycle: $t/T = 0$ (a1)–(a4), 0.25 (b1)–(b4), 0.5 (c1)–(c4), and 0.75 (d1)–(d4), during a flapping cycle. The upper two rows display the data on the symmetry plane from a lateral perspective, while the lower two rows offer a top–down view.

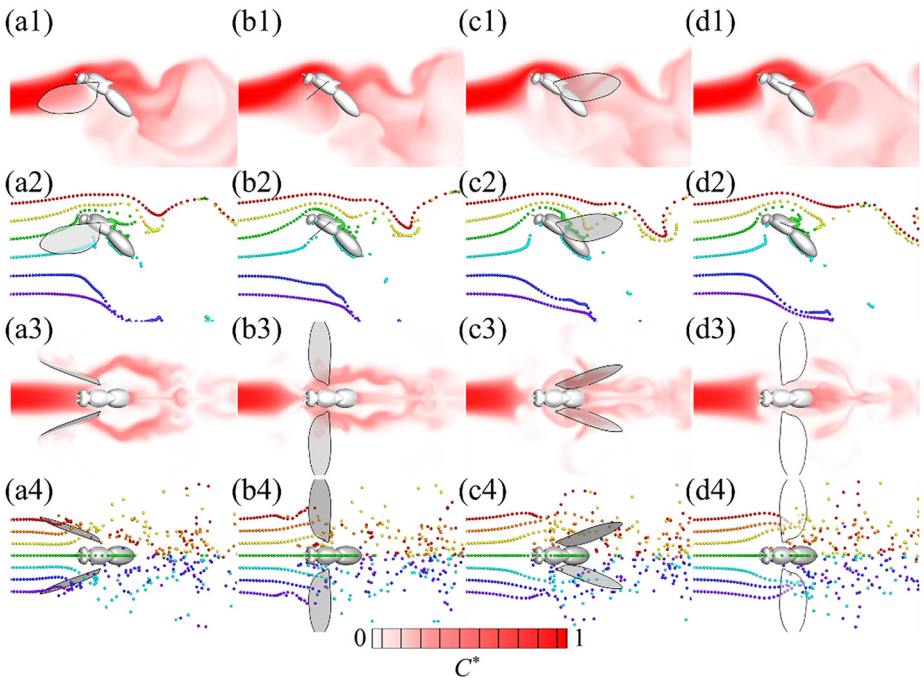

FIG. 28. Odor concentration field (first and third rows) and streaklines (second and fourth rows) for the $Re = 360$ case at four key instants during a flapping cycle: $t/T = 0$ (a1)–(a4), 0.25 (b1)–(b4), 0.5 (c1)–(c4), and 0.75 (d1)–(d4), during a flapping cycle. The upper two rows display the data on the symmetry plane from a lateral perspective, while the lower two rows offer a top–down view.

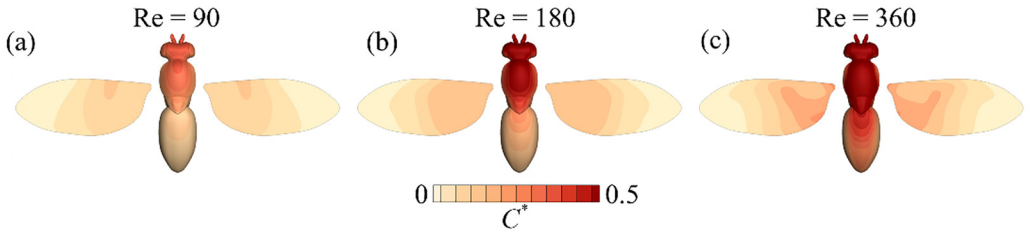

FIG. 29. Odor concentration distribution on the back of the fruit fly model for $Re = 90$ (a), 180 (b), and 360 (c).

Our results demonstrate a strong correlation between reduced frequency and odor perception, both in terms of timing and intensity. At lower reduced frequencies, which correspond to higher forward velocities, the wing-induced flow orchestrates a unique 'saddle point' that optimally elevates the odor plume above the antennae during the downstroke, only to guide it back during the upstroke. This results in a heightened sensitivity to odors during downstrokes and reduced sensitivity during upstrokes. Conversely, at higher reduced frequencies associated with slower forward motion, the wing-induced flow is powerful enough to create a stagnation point alongside the saddle point, effectively forming a 'shield' of airflow. This shield obstructs direct frontal odor reception but amplifies the area from which odors can be sensed. This aerodynamic phenomenon may elucidate why insects demonstrate varied flight patterns—surging upwind at higher speeds and zigzagging at lower speeds—when searching for an odor source. Moreover, the Reynolds number was found to have a significant influence on both the flow field and odor landscape. A higher Reynolds number enhances odor sensitivity due to increased odor diffusivity and more potent wing-induced flow dynamics. While our simulations are subject to the limitations of restricted wing and body kinematics, the insights gained hold considerable promise for the engineering of man-made, odor-guided micro air vehicles. These findings pave the way for bio-inspired designs that can more accurately replicate the efficient and nuanced odor-tracking strategies observed in insects.

ACKNOWLEDGMENTS

This research was supported by the National Science Foundation (CBET-2042368) to C. Li, monitored by Dr. R. D. Joslin. All simulations were run on the High-Performance Computing Cluster of the College of Engineering at Villanova University.

AUTHOR DECLARATIONS

Conflict of Interest

The authors have no conflicts to disclose.

Author Contributions

Menglong Lei: Data curation (equal); Formal analysis (equal); Investigation (equal); Methodology (equal); Validation (equal); Visualization (equal); Writing – original draft (lead). **Chengyu Li:** Conceptualization (equal); Formal analysis (equal); Funding acquisition (lead); Investigation (equal); Supervision (lead); Writing – review & editing (lead).

DATA AVAILABILITY

The data that support the findings of this study are available from the corresponding author upon reasonable request.

REFERENCES

[1]M. A. Willis, "Chemical plume tracking behavior in animals and mobile robots," Navigation **55**, 127 (2008).
[2]J. L. Talley, E. B. White, and M. A. Willis, "A comparison of odor plume-tracking behavior of walking and flying insects in different turbulent environments," J. Exp. Biol. **226**, jeb244254 (2023).
[3]A. Gomez-Marin, B. Duistermars, M. A. Frye, and M. Louis, "Mechanisms of odor-tracking: Multiple sensors for enhanced perception and behavior," Front. Cell. Neurosci. **4**, 6 (2010).
[4]A. F. Carey, G. Wang, C.-Y. Su, L. J. Zwiebel, and J. R. Carlson, "Odorant reception in the malaria mosquito Anopheles gambiae," Nature **464**, 66 (2010).
[5]A. Egea-Weiss, A. Renner, C. J. Kleineidam, and P. Szyszka, "High precision of spike timing across olfactory receptor neurons allows rapid odor coding in Drosophila," iScience **4**, 76 (2018).
[6]P. Szyszka, R. C. Gerkin, C. G. Galizia, and B. H. Smith, "High-speed odor transduction and pulse tracking by insect olfactory receptor neurons," Proc. Natl. Acad. Sci. U.S.A. **111**, 16925 (2014).
[7]K. Parthasarathy and M. Willis, "Spatial odor discrimination in the hawkmoth, *Manduca sexta* (L.)," Biol. Open **10**, bio058649 (2021).
[8]M. A. Willis, E. Ford, and J. Avondet, "Odor tracking flight of male *Manduca sexta* moths along plumes of different cross-sectional area," J. Comp. Physiol., A **199**, 1015 (2013).
[9]R. Pang, F. van Breugel, M. Dickinson, J. A. Riffell, and A. Fairhall, "History dependence in insect flight decisions during odor tracking," PLoS Comput. Biol. **14**, e1005969 (2018).
[10]M. Geier, O. J. Bosch, and J. Boeckh, "Influence of odour plume structure on upwind flight of mosquitoes towards hosts," J. Exp. Biol. **202**, 1639 (1999).
[11]A. Mafra-Neto and R. T. Cardé, "Fine-scale structure of pheromone plumes modulates upwind orientation of flying moths," Nature **369**, 142 (1994).
[12]F. van Breugel and M. H. Dickinson, "Plume-tracking behavior of flying Drosophila emerges from a set of distinct sensory-motor reflexes," Curr. Biol. **24**, 274 (2014).
[13]B. T. Michaelis, K. W. Leathers, Y. V. Bobkov, B. W. Ache, J. C. Principe, R. Baharloo, I. M. Park, and M. A. Reidenbach, "Odor tracking in aquatic organisms: The importance of temporal and spatial intermittency of the turbulent plume," Sci. Rep. **10**, 7961 (2020).
[14]T. J. Steele, A. J. Lanz, and K. I. Nagel, "Olfactory navigation in arthropods," J. Comp. Physiol., A **209**, 467 (2023).
[15]C. P. Ellington, C. van den Berg, A. P. Willmott, and A. L. R. Thomas, "Leading-edge vortices in insect flight," Nature **384**, 626 (1996).
[16]M. H. Dickinson, F. O. Lehmann, and S. P. Sane, "Wing rotation and the aerodynamic basis of insect flight," Science **284**, 1954 (1999).
[17]R. J. Bomphrey, T. Nakata, N. Phillips, and S. M. Walker, "Smart wing rotation and trailing-edge vortices enable high frequency mosquito flight," Nature **544**, 92 (2017).
[18]S. P. Sane and N. P. Jacobson, "Induced airflow in flying insects II. Measurement of induced flow," J. Exp. Biol. **209**, 43 (2006).

[19]C. Loudon and M. Koehl, "Sniffing by a silkworm moth: Wing fanning enhances air penetration through and pheromone interception by antennae," J. Exp. Biol. **203**, 2977 (2000).
[20]K. R. Mylne and P. Mason, "Concentration fluctuation measurements in a dispersing plume at a range of up to 1000 m," Q. J. R. Meteorol. Soc. **117**, 177 (1991).
[21]K. R. Mylne, "Concentration fluctuation measurements in a plume dispersing in a stable surface layer," Boundary-Layer Meteorol. **60**, 15 (1992).
[22]P. A. Moore and J. Atema, "Spatial information in the three-dimensional fine structure of an aquatic odor plume," Biol. Bull. **181**, 408 (1991).
[23]C. Li, "Effects of wing pitch kinematics on both aerodynamic and olfactory functions in an upwind surge," Proc. Inst. Mech. Eng., Part C **235**, 296 (2021).
[24]C. Li, H. Dong, and K. Zhao, "Dual functions of insect wings in an odor-guided aeronautic navigation," J. Fluids Eng. **142**, 030902 (2020).
[25]C. Li, H. Dong, and K. Zhao, "A balance between aerodynamic and olfactory performance during flight in Drosophila," Nat. Commun. **9**(1), 3215 (2018).
[26]M. Lei and C. Li, "Numerical investigation of the passive pitching mechanism in odor-tracking flights," AIAA Paper No. 2020-3016, 2020.
[27]S. N. Fry, R. Sayaman, and M. H. Dickinson, "The aerodynamics of free-flight maneuvers in Drosophila," Science **300**, 495 (2003).
[28]A. J. Bergou, L. Ristroph, J. Guckenheimer, I. Cohen, and Z. J. Wang, "Fruit flies modulate passive wing pitching to generate in-flight turns," Phys. Rev. Lett. **104**, 148101 (2010).
[29]H. Wan, H. Dong, and G. P. Huang, "Hovering hinge-connected flapping plate with passive deflection," AIAA J. **50**, 2020 (2012).
[30]C. Li, H. Dong, and B. Cheng, "Effects of aspect ratio and angle of attack on tip vortex structures and aerodynamic performance for rotating flat plates," AIAA Paper No. 2017-3645, 2017.
[31]H. Wan, H. Dong, C. Li, and Z. Liang, "Vortex formation and aerodynamic force of low aspect-ratio plate in translation and rotation," AIAA Paper No. 2012-3278, 2012.
[32]C. Li, H. Dong, and B. Cheng, "Tip vortices formation and evolution of rotating wings at low Reynolds numbers," Phys. Fluids **32**, 021905 (2020).
[33]J. Wang, C. Li, R. Zhu, G. Liu, and H. Dong, "Wake structure and aerodynamic performance of passively pitching revolving plates," AIAA Paper No. 2019-1376, 2019.
[34]C. Li and H. Dong, "Three-dimensional wake topology and propulsive performance of low-aspect-ratio pitching-rolling plates," Phys. Fluids **28**, 071901 (2016).
[35]C. Li, H. Dong, and G. Liu, "Effects of a dynamic trailing-edge flap on the aerodynamic performance and flow structures in hovering flight," J. Fluid Struct. **58**, 49 (2015).
[36]J. Wang, C. Li, Y. Ren, and H. Dong, "Effects of surface morphing on the wake structure and performance of flapping plates," AIAA Paper No. 2017-3643, 2017.
[37]C. Li and H. Dong, "Quantification and analysis of propulsive wake topologies in finite aspect-ratio pitching-rolling plates," AIAA Paper No. 2016-4339, 2016.
[38]M. Xu, M. Wei, C. Li, and H. Dong, "Adjoint-based optimization for thrust performance of three-dimensional pitching–rolling plate," AIAA J. **57**, 3716 (2019).
[39]C. Li and H. Dong, "Wing kinematics measurement and aerodynamics of a dragonfly in turning flight," Bioinspiration Biomimetics **12**, 026001 (2017).
[40]H. Dong, A. T. Bode-Oke, and C. Li, *Learning from Nature: Unsteady Flow Physics in Bioinspired Flapping Flight* (InTech, 2018).
[41]S. Lionetti, T. L. Hedrick, and C. Li, "Numerical investigation of olfactory performance in upwind surging hawkmoth flight," AIAA Paper No. 2023-4242, 2023.
[42]Z. Lou and C. Li, "Unsteady aerodynamics and wake structures of butterfly in forward flight," AIAA Paper No. 2023-4241, 2023.
[43]R. Mittal, H. Dong, M. Bozkurttas, F. Najjar, A. Vargas, and A. Von Loebbecke, "A versatile sharp interface immersed boundary method for incompressible flows with complex boundaries," J. Comput. Phys. **227**, 4825 (2008).
[44]S. Lionetti, T. L. Hedrick, and C. Li, "Aerodynamic explanation of flight speed limits in hawkmoth-like flapping-wing insects," Phys. Rev. Fluids **7**, 093104 (2022).
[45]Y. Liu, A. D. Lozano, T. L. Hedrick, and C. Li, "Comparison of experimental and numerical studies on the flow structures of hovering hawkmoths," J. Fluid Struct. **107**, 103405 (2021).
[46]C. Lee, Z. Su, H. Zhong, S. Chen, M. Zhou, and J. Wu, "Experimental investigation of freely falling thin disks. Part 2. Transition of three-dimensional motion from zigzag to spiral," J. Fluid Mech. **732**, 77 (2013).
[47]A. J. Bergou, S. Xu, and Z. J. Wang, "Passive wing pitch reversal in insect flight," J. Fluid Mech. **591**, 321 (2007).
[48]M. Lei and C. Li, "The aerodynamic performance of passive wing pitch in hovering flight," Phys. Fluids **32**, 051902 (2020).
[49]M. Lei and C. Li, "A balance between odor intensity and odor perception range in odor-guided flapping flight," in Proceedings of the Fluids Engineering Division Summer Meeting, 2022, Paper No. FEDSM 2022-85840.
[50]D. Ishihara, Y. Yamashita, T. Horie, S. Yoshida, and T. Niho, "Passive maintenance of high angle of attack and its lift generation during flapping translation in crane fly wing," J. Exp. Biol. **212**, 3882 (2009).
[51]C. Li, J. Wang, G. Liu, X. Deng, and H. Dong, "Passive pitching mechanism of three-dimensional flapping wings in hovering flight," in Proceedings of the ASME-JSME-KSME 2019 8th Joint Fluids Engineering Conference, 2019, Paper No. AJKFluids 2019-4639.
[52]M. Lei, J. P. Crimaldi, and C. Li, "Navigation in odor plumes: How do the flapping kinematics modulate the odor landscape?," AIAA Paper No. 2021–2817, 2021.
[53]M. Lei and C. Li, "Effects of wing kinematics on modulating odor plume structures in the odor tracking flight of fruit flies," in Proceedings of the Fluids Engineering Division Summer Meeting, 2021, Paper No. FEDSM 2021-61832.
[54]X. Meng, Y. Liu, and M. Sun, "Aerodynamics of ascending flight in fruit flies," J. Bionic Eng. **14**, 75 (2017).
[55]S. N. Fry, R. Sayaman, and M. H. Dickinson, "The aerodynamics of hovering flight in Drosophila," J. Exp. Biol. **208**, 2303 (2005).